HHS Public Access

Author manuscript

Nat Neurosci. Author manuscript; available in PMC 2024 June 27.

Published in final edited form as:

Nat Neurosci. 2023 September ; 26(9): 1642–1650. doi:10.1038/s41593-023-01408-2.

High-speed multi-plane confocal microscopy for voltage imaging in densely labeled neuronal populations

Timothy D. Weber[1,*], **Maria V. Moya**[1,2,*], **Kıvılcım Kılıç**[1,3], **Jerome Mertz**[1,2,3,4,†], **Michael N. Economo**[1,2,3,4,†]

[1]Department of Biomedical Engineering, Boston University, Boston, MA

[2]Center for Systems Neuroscience, Boston University, Boston, MA

[3]Neurophotonics Center, Boston University, Boston, MA

[4]Photonics Center, Boston University, Boston, MA

Abstract

Genetically encoded voltage indicators (GEVIs) hold immense potential for monitoring neuronal population activity. To date, best-in-class GEVIs rely on one-photon excitation. However, GEVI imaging of dense neuronal populations remains difficult because out-of-focus background fluorescence produces low contrast and excess noise when paired with conventional one-photon widefield imaging methods. To address this challenge, we developed a novel imaging system capable of efficient, high-contrast GEVI imaging at near-kHz rates and demonstrate it for in vivo and ex vivo imaging applications in the mouse neocortex. Our approach uses simultaneous multiplane imaging to monitor activity within contiguous tissue volumes with no penalty in speed or requirement for high excitation power. This approach, Multi-Z Imaging with Confocal detection (MuZIC), permits high signal-to-noise ratio voltage imaging in densely labeled neuronal populations and is compatible with imaging through micro-optics. Moreover, it minimizes artifacts associated with concurrent imaging and optogenetic photostimulation for all-optical electrophysiology.

INTRODUCTION

Optical measurement of activity across neuronal populations with genetically encoded calcium indicators (GECIs), such as the GCaMPs[1–3], has been invaluable for studying

mne@bu.edu .

*These authors contributed equally

†These authors jointly supervised this work

AUTHOR CONTRIBUTIONS

T.D.W., M.V.M., J.M., and M.N.E. conceived of the project. M.N.E. and J.M. supervised research. T.D.W., J.M., and M.N.E. designed the MuZIC system. M.V.M., K.K., and M.N.E. prepared samples. T.D.W., M.V.M., K.K., and M.N.E. performed experiments. T.D.W., M.V.M., and M.N.E. analyzed data. T.D.W. performed simulations. T.D.W., M.V.M., J.M., and M.N.E. wrote the manuscript.

CODE AVAILABILITY

All code used for data analyses are provided on Figshare (DOI: 10.6084/m9.figshare.23542167).

COMPETING INTERESTS

J.M., T.D.W., and Boston University have a US patent filed (#11,042,016) that relates to multiplane confocal imaging. The remaining authors declare no competing interests.

neural dynamics with cell type specificity[4,5]. However, GECI fluorescence is nonlinearly related to neural activity, does not report subthreshold voltage changes, and does not have temporal resolution sufficient to track many of the fast neural processes associated with naturalistic behavior[1,6,7]. Genetically encoded voltage indicators[8–13] (GEVIs) have the potential to address these shortcomings[14]. However, GEVI imaging poses two key challenges for microscope design. First, action potentials and other changes in membrane voltage occur on a time scale of milliseconds, requiring near-kilohertz sampling rates. Second, the fractional change in fluorescence of best-in-class GEVIs in response to physiological voltage fluctuations remains small compared to widely used GECIs – typically less than 10%. Effective voltage imaging thus requires an imaging system that can provide high signal-to-noise ratio (SNR) measurements at near-kilohertz frame rates.

To meet this requirement, voltage imaging can be conducted using single-photon widefield imaging with fast (0.1–1 kHz) sCMOS cameras. However, fluorescent signal originating from the focal plane of a widefield microscope can be overwhelmed by out-of-focus background in thick tissues. To reduce out-of-focus background fluorescence, GEVIs can be expressed in a small subset of neurons and imaging can be performed with the aid of targeted illumination[8,11,15]. This permits widefield imaging of single neurons, although out-of-focus background still degrades the SNR of fluorescence measurements. Alternatively, fast two-photon imaging can be used to reduce out-of-focus background fluorescence but can be technically complex and can require sparse labeling and/or excitation powers that risk tissue heating[11,12,16,17]. Two-photon excitation also renders widely used rhodopsin-based GEVIs[8–10,13,18] voltage-insensitive[8,19,20].

Here, we describe a fast, volumetric confocal microscope designed for GEVI imaging and demonstrate that confocal microscopy provides fundamental advantages over widefield microscopy. Our approach, Multi-Z Imaging with Confocal detection (MuZIC), provides both optical sectioning (background rejection) for increased SNR, and simultaneous high-contrast contiguous multiplane imaging that multiplies the number of neurons that can be imaged without requiring an increase in scanning speed or laser power compared to single-plane imaging[21,22]. Three-dimensional imaging in MuZIC also provides resiliency to sample motion, a major concern in some fast imaging approaches[12]. We demonstrate high-SNR volumetric GEVI imaging of densely labeled neurons in the mouse brain with MuZIC, both *in vitro* and *in vivo*. *In vivo*, MuZIC permits imaging in layer 2/3 noninvasively and across cortical layers with implanted optics. Finally, background light rejection provided by pinholed detectors in MuZIC reduces optical crosstalk during simultaneous voltage imaging and optogenetic stimulation, facilitating simultaneous observation and manipulation of neural activity.

RESULTS

We sought to develop a fluorescence imaging system for voltage imaging that (1) achieves kHz frame rates, (2) maintains high SNR when imaging densely labeled neural populations, (3) minimizes artifacts introduced by optogenetic stimulation and brain motion, and (4) is compatible with rhodopsin-based GEVIs[8–10,13,18]. Currently, rhodopsin-based GEVIs become unresponsive to voltage changes after undergoing two-photon excitation[8,19,20] and

so we focused on single-photon imaging methods. We further focused on confocal imaging due to its excellent optical sectioning. Confocal imaging relies upon point scanning that typically limits frame rates to less than 10 Hz with linear galvanometric scanners and on the order of 100 Hz with resonant galvanometric or spinning disk scanning. Random-access imaging[12,23–27] can achieve faster imaging rates but is sensitive to artifacts introduced by sample motion[12,27], which is particularly problematic when imaging GEVIs that report membrane potential dynamics with small fractional changes in fluorescence and is not straightforward to employ in conjunction with one-photon imaging.

To achieve kilohertz frames rates for GEVI imaging, MuZIC incorporates an ultrafast polygon scanner for the fast axis (x-axis; Fig. 1a). A 128-facet polygon scanner rotating at 54,945 rotations per minute provides a line rate of 117 kHz, an order of magnitude faster than resonant galvanometers. While small facet-to-facet variation in reflectivity and flatness in polygon scanners can introduce frame-to-frame variability in intensity measurements, this issue can be circumvented by ensuring that the same facet scans the same line on each frame. 127-line imaging with the turnaround of the y-axis scanner confined to the time when the 128th facet is rotated into the excitation path thereby eliminates facet-induced noise. With MuZIC, one frame is therefore acquired per rotation of the polygon (128 lines), yielding a frame rate of 916 Hz while avoiding polygon-induced artifacts.

MuZIC incorporates a volumetric confocal strategy that we developed in previous work[21,22] to maximize both the number of neurons that can be imaged and the capture of per-cell fluorescence (rather than only fluorescence emitted from the portion of each cell intersecting a thin optical section) to ensure high SNR. To achieve volumetric confocal imaging, MuZIC uses low-NA excitation to illuminate an extended volume (Fig. 1b, *left*) while maintaining micron-scale resolution laterally. Images of multiple planes within this volume are formed by high-NA fluorescence collection and detection through multiple axially distributed pinholes (Fig. 1a,b). Pinholes in a reflective substrate guide light emitted from outside of the focal plane of one detector to the next pinholed detector, and so forth, enabling simultaneous multiplane imaging (Fig. 1a,b, EDFig. 1). In contrast to our previous multi-Z design, MuZIC employs relatively large pinhole diameters and spacings that minimize ‘dead space’ between planes, yielding efficient light collection throughout a contiguous 150×150×45 μm volume (12 μm inter-plane spacing) while maintaining micron-scale resolution (~2 μm FWHM; EDFig. 2). We evaluated whether MuZIC could provide high-contrast multiplane imaging in fixed samples containing a membrane-bound fluorescent protein. As predicted, MuZIC substantially reduces background fluorescence that otherwise degrades SNR during widefield imaging (Fig. 1c).

Although confocal microscopy requires similar average illumination light intensity to widefield microscopy, the requirement for point scanning in confocal microscopy imposes much higher instantaneous illumination intensities, by a factor A_{FOV}/A_0 (~7000× in our system), where A_{FOV} and A_0 are the FOV and excitation focal spot areas respectively. We examined whether fluorescence saturation limits our ability to obtain high-SNR GEVI measurements[28]. For the GEVI Voltron2[9], we determined that the required illumination intensity for MuZIC imaging is well below the saturation level by at least an order of magnitude (Supplementary Note 1), and that MuZIC is therefore readily compatible

with GEVI imaging. Notably, MuZIC provides multiplane imaging 'for free' – there is no requirement for increased illumination power – and intentionally uses a focal spot diameter somewhat larger than in standard confocal microscopy, further reducing the risk of fluorescence saturation (Supplementary Note 1).

To establish the effectiveness of MuZIC for GEVI imaging, we first labeled neurons in the mouse motor cortex with soma-targeted Voltron2-ST_{JF585} and performed simultaneous whole-cell electrophysiology and MuZIC imaging in acute brain slices *in vitro*. In densely labeled samples, thirty to forty neurons could be clearly discerned across four focal planes with high contrast (Fig. 1d). These numbers are on par with those reported with widefield imaging of sparsely labeled neurons, and approximately an order of magnitude more than typically reported with two-photon voltage imaging[11,12,16,17]. Action potentials and subthreshold voltage fluctuations (Fig. 2a) induced by intracellular current injection were readily detected in single trials using the same average illumination intensity (~10 mW/mm^2; Supplementary Table 1) commonly employed in widefield imaging experiments. Averaging across trials revealed small, subthreshold changes in membrane potential (Fig. 2b). We further found a linear relationship between voltage and fluorescence in Voltron2-ST_{JF585}-labeled neurons that was consistent across neurons (Fig. 2c,d; 0.19 ± 0.04 % per mV, n = 14 cells).

To determine whether MuZIC permits dense GEVI imaging *in vivo*, we examined mice in which neurons in the motor cortex were densely labeled with Voltron2-ST_{JF552}, noting that JF552 crosses the blood brain barrier more effectively than JF585. Most individual cells could not be resolved with widefield imaging (Fig. 3a) but could be visualized with high contrast with MuZIC (Fig. 3a, *right*). *In vivo* imaging in awake mice revealed fluorescence transients corresponding to spontaneous action potentials in multiple neurons simultaneously as well their subthreshold voltage dynamics (Fig. 3b), which were characterized by transient periods of high correlation (Fig. 3b). Multiplane imaging remained effective in vivo (Fig. 3c). Cells located at different axial positions could be simultaneously imaged, as *in vitro*, and often spanned multiple planes, allowing us to maximize light collection from single cells while minimizing photobleaching (EDFig. 3). Moreover, volumetric imaging provided resilience to axial brain motion. During periods of axial sample motion, cells were observed to dim and brighten in opposition in adjacent planes in such a way that total collected fluorescence across planes varied substantially less than fluorescence collected in individual planes (EDFig. 4).

We found that high-SNR *in vivo* imaging was typically possible in neocortical layer II, at depths of 150 – 200 μm, enabling us to effectively monitor the subthreshold and/or spiking dynamics of cortical pyramidal neurons (Fig. 4). To quantitatively assess the depth dependence of voltage imaging with MuZIC, we measured the average fluorescence intensity across a sample of cells (n = 52 cells, 8 FOVs, 5 animals; 51–215 μm from the pial surface; Fig. 4b, *left*) at a constant illumination intensity of 6.75 mW (the maximum for our source). We also quantified the contrast, estimated spike SNR, and photobleaching rate for the same set of cells (Fig. 4b, *middle and right*). From fits to these data (*dashed lines*), we estimate that average spike SNR decreases by 30.5% per 100 μm in depth (from 6.2 at 50 μm to 4.3 at 150 μm). This decrease in SNR is primarily driven by a decrease in fluorescence

power (46.2% per 100 μm; from 9078 to 4882 photons/cell/frame between 50 and 150 μm) rather than a drop in contrast, which decreased only modestly, (8.5%; 0.72 to 0.66 between 50 and 150 μm). Importantly, the photobleaching rate also decreased with depth (39.3%; from 0.030 to 0.018 between 50 and 150 μm), indicating reduced excitation power at the focus due to absorption and scattering along the beam path. Increasing illumination power with depth to account for reduced fluorescence excitation, as is customary with *in vivo* two-photon imaging, would permit higher SNR imaging at depth than we demonstrate here.

These data demonstrate that MuZIC enables high-SNR voltage imaging in neocortical layer 2/3. Because noninvasive voltage imaging in deeper cortical layers and deeper brain regions is not currently possible using any existing imaging modality, we also tested compatibility of MuZIC imaging with implantable optics. We found that applying MuZIC in combination with an implanted reflecting microprism[29] allowed *in vivo* imaging across cortical layers (Fig. 5), revealing voltage dynamics even in layer 5b pyramidal tract neurons (Fig. 5b,c) – to our knowledge reported for the first time here.

We observed that, as expected, imaging through high-refractive-index cranial windows and implantable optics induced spherical aberrations, which in turn reduced the optical sectioning strength compared to *in vitro* imaging. Nevertheless, without any aberration correction, neuronal somata and proximal dendritic processes remained easily resolvable (Fig. 5b), and numerical simulations indicate that overall collection efficiency – and thus SNR – remains minimally affected even when aberrations are large due to the close axial spacing and relatively large size of the pinholes employed in MuZIC (EDFig. 5). In principle, these aberrations could be corrected with compensation optics to recover any loss of axial resolution.

Next, we evaluated the suitability of MuZIC for all-optical physiology[13,30,31], in which GEVI imaging is combined with optogenetic photostimulation for simultaneous measurement and open- or closed-loop control of neural activity. While all-optical physiology represents a powerful emerging method for non-invasively interrogating neural circuit function, light used for optogenetic stimulation can corrupt voltage imaging signals if it cannot be fully separated spectrally or stimulates emission from autofluorescent species within tissue. Detection of even small amounts of stimulation light can induce significant optical artifacts on the same order as physiological changes in neuronal voltage. Unlike widefield and two-photon microscopy, which collect light indiscriminately, confocal detection rejects light emitted from sources outside of the focal area, making it well-suited for all-optical physiology. The field-of-view and pinhole diameters employed in MuZIC yield a ~1,000-fold reduction in detection of full-field photostimulation light compared to widefield and two-photon imaging (Supplementary Note 2).

To experimentally demonstrate all-optical physiology without optical artifacts using MuZIC, we co-expressed the optogenetic activator channelrhodopsin (ChR2) and the GEVI Voltron2-ST_{JF585} in overlapping subsets of cortical neurons and applied blue-light stimulation to simultaneously manipulate and record neural activity *in vitro* (Fig. 6a). Action potentials and subthreshold depolarizations could be readily detected across populations of neurons (Fig. 6b). Prolonged (400 ms) blue-light stimulation induced subthreshold depolarization

and trains of action potentials in doubly infected neurons without optical artifacts (Fig. 6b). Brief (1 ms) blue-light stimuli induced action potentials with variable latency on a subset of trials and subthreshold depolarizations on the remaining trials (Fig. 6c,d). Subtle features of the voltage responses to optogenetic stimulation, such as spike afterhyperpolarizations, could also be tracked optically (Fig. 6c,d). Together, these data demonstrate the potential for artifact-free, all-optical physiology in densely labeled neural populations with MuZIC. We note that our 561 nm light source produced modest off-target excitation of ChR2, leading to 1–10 mV depolarization of cells upon imaging, although this might be mitigated by employing an opsin with blue-shifted excitation[13] and/or imaging with a longer-wavelength (594 nm) source.

Finally, we sought to understand quantitatively how labeling density affects the relationship between SNR in confocal and widefield microscopy. Confocal microscopy provides a distinct SNR advantage over widefield microscopy because it rejects background fluorescence. However, confocal (and two-photon) microscopy require fast photodetectors that typically provide only modest quantum efficiency (QE). Confocal detection also partially rejects desired signal to an extent that depends upon the chosen pinhole size. MuZIC employs silicon photomultiplier (SiPM) detectors (QE: ~40%) with roughly half the sensitivity of sCMOS cameras (QE: ~80%). When a neuronal soma spans multiple planes, approximately ~1/3 of the total emitted fluorescence is rejected by the pinholes (EDFig. 5). Taking these factors into account, we find that the SNR of confocal microscopy begins to surpass that of widefield microscopy when the ratio of out-of-focus background fluorescence to in-focus signal (background-to-signal ratio; BSR) is larger than 3 (Supplementary Note 3; EDFig. 6a). We examined BSR of Voltron2-labeled neurons *in vivo*, by injecting high-titer AAV-FLEX-Voltron2-ST and low-titer AAV-Cre (see Methods) into layer 2/3 of the somatosensory cortex to express the sensor in a subset of cortical neurons. In the penumbra of the injection site, where cells were sparsely labeled, individual cells could be resolved with widefield imaging and were found to have a BSR of ~5–20 (EDFig. 6b). Near the center of the injection site, individual cells could not be clearly resolved with widefield imaging (EDFig. 6b). We also examined data from a previously published study in which Voltron was expressed extremely sparsely in interneurons confined only to layer 1[8] – approaching the limit of low background – and found BSR to be 1.3 ± 0.4 (mean ± s.d.; n = 18 cells), slightly below the break-even point. Thus, MuZIC provides an SNR advantage over widefield imaging for most – but not all – labeling densities *in vivo*.

A common method for reducing BSR in widefield microscopy is to make use of targeted illumination, where excitation light is spatially patterned with a digital micromirror device (DMD) or spatial light modulator (SLM) to illuminate only cells of interest[8,11,15]. To determine how BSR is reduced by widefield imaging with targeted illumination, we measured signal and background levels when only a single cell-sized spot (25 μm) was illuminated (Supplementary Note 4; EDFig 6c). Single-spot illumination approaches confocal excitation and represents the lower bound of achievable BSR with targeted illumination. In this case, we found that targeted illumination reduced background by a factor of approximately 5, in line with recent measurements in the mouse hippocampus[11], leading to an increase in the breakeven BSR by the same value (Supplementary Note 4). Depending on the number of cells targeted, the break-even BSR varies between 3 (entire

field illuminated) and 15 (single cell illuminated; EDFig. 6d). In densely labeled regions, individual cells could not be resolved by widefield microscopy and therefore targeted illumination of densely labeled neurons (i.e. where BSR exceeds ~20) could not be assessed. In contrast, single neurons remain easily resolvable in confocal microscopy regardless of label density.

DISCUSSION

We have demonstrated that MuZIC enables high-contrast, volumetric GEVI imaging *in vitro* and *in vivo.* In MuZIC, confocal detection rejects background fluorescence which otherwise prohibits widefield imaging in densely labeled samples. Fast polygonal scanning enables near-kilohertz imaging while extended illumination combined with an array of pinholed detectors allows multiple focal planes to be imaged simultaneously without the need for additional excitation power and increased photodamage. These features multiply the number of neurons that can be imaged and reduce sensitivity to axial sample motion. Pinholed detectors also minimize artifacts associated with simultaneous optogenetic stimulation by three orders of magnitude, facilitating all-optical physiology. MuZIC systems can be built with readily available optical components and freely available software for a total cost on par with commonly used widefield microscopes – and far less than systems employing two-photon excitation. Additionally, we have established that confocal imaging provides a fundamental benefit in SNR over widefield imaging in densely labeled tissues, even when widefield is combined with targeted illumination.

Realizing the advantages of confocal microscopy for GEVI imaging requires careful design. For example, all point-scanning methods run the risk of fluorescence excitation saturation[28,32], particularly high-resolution methods where an excitation beam is tightly focused. Here, we use low-NA excitation to achieve an axially extended focus for multiplane imaging and larger pinholes (~4 Airy units) for increased collection efficiency. These modifications purposefully reduce resolution compared to conventional (single-plane) confocal microscopy to avoid molecular saturation and increase the number of per-cell GEVI indicators contained within each focal volume. Although higher resolution multiplane imaging could be obtained, for example, with Bessel-beam or multi-focus excitation with a diffractive optical element, this would require increased sampling speed (and hence reduced sampling time) to maintain similar frame rate and FOV, while also increasing the risk of excitation saturation. Further, we optimized pinhole diameter and spacing to minimize the ‘dead-space’ between detection planes where fluorescence emission would be rejected by all pinholes. This approach provided continuous volumetric imaging, maximized fluorescence collected from each neuron within the focal volume, and minimized artifacts associated with axial brain motion *in vivo*. Notably, the number of planes in our system (4) was set by our detection electronics but could readily be increased by adding detection channels, thus increasing effective FOV at no cost in speed or excitation power.

Despite incorporating larger pinholes than typically employed in confocal microscopy, MuZIC provides higher contrast than widefield microscopy, even when illumination is targeted to individual somata of interest (EDFig. 6, Supplementary Notes 3,4). The high contrast afforded by confocal detection is not only important for reducing shot noise so as to

increase SNR, but also reduces 'optical cross talk' between cells, in which scattered or out-of-focus photons emitted by sensor proteins associated with one cell are misattributed to a different cell. Crosstalk can corrupt measurements of membrane voltage and lead to spurious conclusions about the activity of single neurons. To reduce crosstalk, two-photon imaging of cytosolic calcium indicators in *vivo* often requires an ad hoc procedure for 'neuropil subtraction' to computationally remove signals associated with axons and dendrites near somata of interest. Here, we observe a marked absence of optical crosstalk due both to the high contrast provided by confocal detection in MuZIC and the perisomatic targeting of Voltron2, which reduces neuropil labeling. MuZIC imaging of densely labeled cells faithfully reports single-neuron activity, as measured electrophysiologically, even during full-field optogenetic stimulation that induces highly synchronous population activity (Fig. 6). A potential drawback of fast point-scanning with polygon scanners is their limited, fixed scan angle, which sets the field of view along one axis. In our system, a 128-facet polygon limited the field of view size in the X-direction to 150 μm. However, in the Y-direction, the number of lines acquired within each image is unconstrained and linearly related to the frame period. Thus, it is possible to increase the field-of-view size along the Y-direction so long as the number of acquired lines remains a multiple or divisor of the number of polygon facets to avoid artifacts associated with facet-to-facet variability. This approach could be especially useful for applications focused on measurement of subthreshold voltage fluctuations, rather than neuronal spiking, due to their slower dynamics.

Another potential drawback of confocal microscopy, as a single-photon imaging modality, is its limited depth penetration in scattering tissue. We note that conventional confocal microscopes are typically designed to achieve high spatial resolution with high-NA excitation, small pinhole sizes, making them particularly susceptible to loss of signal with increased depth penetration. By purposefully making use of increased pinhole sizes, MuZIC benefits from larger probe volumes at the expense of resolution. We found that high-SNR *in vivo* imaging was possible with MuZIC in cortical layer 2/3, comparable to leading methods for fast two-photon imaging[11,12,16,17]. This is perhaps surprising, given that two-photon methods are often favored over one-photon imaging methods specifically for their enhanced depth penetration. However, fast raster-scanning two-photon methods require several orders of magnitude higher excitation power due to the inefficiency of two-photon excitation. To avoid thermal damage, power density must be constrained, which, in turn, poses a constraint on FOV that becomes more severe with increasing depth. For example, two-photon voltage imaging beyond the depths accessible by MuZIC is typically targeted to one or two neurons at a time, and only for short durations[11,12,16,17]. Random-access two-photon methods using acousto-optic deflectors[11,12,16,17] are less constrained by sample heating, since only cells of interest are illuminated, but are technically challenging to implement, have a limited update rate (limited by the speed of sound) that fundamentally constrains kHz-rate imaging to ~20 cells, and can be highly sensitive to sample motion. Thus far, random access two photon microscopy has typically been restricted to cortical layer 2/3 as well. Moreover, two-photon voltage imaging requires hardware that is an order of magnitude costlier than one-photon methods and cannot be used with many common GEVIs, as they are rendered voltage-insensitive by nonlinear excitation[8,19,20].

Regardless of imaging modality, GEVI imaging in deep cortical layers and deep brain structures requires the use of miniature relay optics embedded within tissue, such as a microprism (Fig. 5) or GRIN lens[29,33,34]. The field-of-view limitations of relay optics accentuate the value of imaging densely labeled neural populations and multiplane imaging, both of which multiply the number of cells that can be visualized within a region of fixed lateral extent. In contrast, single-plane imaging of sparsely labeled neurons severely limits the number of GEVI-expressing cells that can be recorded through relay optics. GEVI imaging can reveal the spiking and subthreshold dynamics of neural populations with millisecond precision and cell-type specificity. This combination of features suggests immense potential for GEVI imaging in applications across systems and cellular neuroscience. Nevertheless, realizing the potential of GEVIs requires the development of new imaging technologies that keep pace with sensor development. To our knowledge, MuZIC represents the first single-photon imaging method with the speed and contrast required for GEVI imaging in densely labeled neural tissues. MuZIC also facilitates simultaneous imaging and optogenetic stimulation so that the neural responses to optogenetic perturbations can be directly measured without optical artifacts. Together, these features promise to make MuZIC a valuable tool for dissecting neural circuit function *in vitro* and *in vivo*.

METHODS

All animal procedures and experiments were carried out with approval from the Boston University Institutional Animal Care and Use Committee (IACUC) and in accordance with National Institutes of Health (NIH) policies and guidelines.

Microscope design

We designed the MuZIC system (Fig. 1a, EDFig. 1) for imaging longer-wavelength JF585 to open the blue spectral window for optogenetic stimulation, reduce tissue autofluorescence, increase penetration depth, and match the fluorescence emission to peak detector sensitivity (600 nm). A 561 nm diode laser (Vortran Stradus 561–50) was used as an excitation source in all experiments. To underfill the objective back aperture, the laser beam diameter was reduced with an iris aperture and reimaged onto a polygonal scanner, which performed the fast axis (x) scanning. The laser beam was coupled into the optical path just before the polygonal scanner via a dichroic mirror (Chroma T570lpxr). The polygon scanner (Lincoln Laser SA-24 with DT-128-250-025-AA protected gold mirror) features 128 facets, rotating at 54,945 RPM, which generated a fast axis scan rate of 117.2 kHz. From the polygonal scanner, the beam was relayed to a galvanometer scanner (Cambridge Technology 6215H), providing the slow axis (y) scan, and relayed again to the back aperture of the objective lens. To generate an axially extended illumination focus, the effective illumination NA was limited to approximately 0.15. All experiments were performed with a 16× 0.8 NA water-immersion objective (Nikon CFI75 LWD 16X W).

Emitted fluorescence was epi-collected, de-scanned, and separated from reflected illumination light with the dichroic mirror and an additional emission filter (Chroma ET570lp). The de-scanned fluorescence was focused onto a set of axially distributed

reflective pinholes (Edmund Optics #45-604, laser ablated by National Aperture). Based on the total estimated lateral magnification (83×), the projected image of each pinhole was 3.6 μm in diameter. The pinholes thus captured the majority of the fluorescence generated from the 4 focal planes. The distance between the focal planes in the sample is given by $z_p n / M^2$ where z_p is the axial distance between the pinholes in image space, n is the refractive index of the sample immersion medium (1.33 for water), and M is the lateral magnification. In our case, $z_p \approx 6$ cm, resulting in a 12 μm interplane spacing in the sample. Care was taken to minimize the angle of incidence (< 17°) on the pinholes such that the projection of the pinhole did not appear elliptical to the oncoming beam.

Red-shifted silicon multipliers (SiPMs, Hamamatsu S14420-1550MG) were selected for their high effective photon detection efficiency (~40%). Each detector was soldered to a custom PCB which included a transimpedance amplification circuit (https://github.com/tweber225/simple-sipm). A reverse bias voltage of 50V was provided with a programmable DC power supply. Amplified signals were digitized and binned to 15 MHz (NI-5734 and NI PXIe-7961) to achieve square, approximately Nyquist-sampled pixels (1.1 μm pixel pitch vs. 2.2 μm PSF mean FWHM). The digitizer was triggered with an external “start of line” signal generated by a laser diode (Thorlabs CPS532) reflected off a separate polygon scanner facet and swept across the sensor of an amplified photodiode (Thorlabs PDA10A).

The system was also equipped with an epi-illumination widefield fluorescence microscopy module for sample navigation. The widefield path could be made available by sliding a repositionable mirror in the scanning path (Thorlabs OPX2400). The module included a green LED (Thorlabs M565L3), a similar filter set (Chroma set 49017), and a CMOS camera (Thorlabs CS165MU), and provided an approximately 0.8×0.6 mm FOV. For *in vitro* experiments, this camera was also combined with an oblique transillumination condenser and a NIR LED to provide phase-gradient contrast for whole-cell patch clamp recordings. Full-field optogenetic stimulation was provided with a blue LED (Thorlabs M470L4) coupled into the scan path via an excitation filter and dichroic mirror (Thorlabs MF475-35 and DMLP505R).

Microscope operation

Scanning and confocal image generation were controlled with ScanImage[35] in combination with Wavesurfer (https://wavesurfer.janelia.org/) to synchronize current injection and optogenetic stimulation. The fast axis scan range was 150 μm (nearly 100% duty cycle) divided into 127 pixels. The slow axis (linear galvanometer) was run in a vertical bi-directional mode. Odd frames were acquired by scanning lines top to bottom, and even frames acquired by scanning bottom to top, a strategy adopted to minimize vertical flyback deadtime. The slow axis scan range and number of lines was matched to the fast axis, yielding 150×150 μm 4-plane imaging at 916 Hz. One additional line scan is required for internal ScanImage synchronization, which brought the total number of fast scans per frame period to 128. Matching t3he fast scans per frame period to a multiple of the polygon facet count eliminates frame-to-frame variation in each acquired line that results from small variations in facet-to-facet pointing and polishing.

For *in vitro* experiments, imaging laser (561 nm) power was set to 0.2–0.9 mW. Over the 0.0225 mm^2 FOV, this is an irradiance 9–40 mW/mm^2, well below the molecular saturation limit for JF585 (Supplementary Note 1)[8,36]. More power (2–6 mW) was required for *in vivo* experiments most likely due to reduced transparency of the optical window and increased absorption by blood and scattering due to deeper imaging. Full-field optogenetic stimulation intensity was adjusted with a neutral density filter and/or LED current control.

Animals

Both male and female C57Bl/6J mice (JAX #000664) and Emx1-IRES-Cre mice (JAX #005628) were used in this study. Fig. 1c also included fixed tissue from a VGAT-Chr2-EYFP mouse (JAX #014548). Mice were housed on a 12-h light/dark cycle at 21±3 degrees Celsius and 30–70% humidity with ad libitum access to food and water

Adult Viral injection

Anesthesia was induced using 5% isoflurane in O_2 and was maintained during surgical procedures using 1–2% isoflurane in O_2. Bupivacaine (0.1 ml, 0.5%) was injected under the skin covering the skull. The skin and periosteum covering the skull were removed and the skull thinned overlying the sites of viral injection(s). For all injections, virus was injected using a manual volume displacement injector (MMO-220A, Narishige) connected to a glass pipette (5-000-2005, Drummond Scientific) pulled to a 30 μm tip (P-2000, Sutter Instruments) that was beveled to a sharp tip. Pipettes were backfilled with mineral oil and virus was front-loaded before injection. Pipettes were inserted through the thinned bone to the appropriate depth and virus injected at 20 nl/min. Animals were injected at 7–9 weeks of age.

Animals were unilaterally injected with a 1:10 dilution of AAV1-hSyn-FLEX-Voltron2-ST-WPRE virus (E. Schreiter) in ALM (coordinates in mm from Bregma: AP +2.5, ML +1.5, DV −1.2 and −0.6) and M1 (from Bregma: AP +0.75, ML +1.5, DV −1.2 and −0.6). Cortical injections to adult C57Bl/6J mice additionally included a 1:250 dilution (for in vitro whole-cell patch experiments) or 1:50 dilution (for in vivo imaging experiments) of rAAVretro-hSyn-Cre (Addgene #105553-AAVrg) to induce expression of Voltron2-ST. Total injection volume at each target site was 100 nL. Mice were administered post-operative sub-cutaneous injections of ketoprofen (5 mg/kg) and buprenorphine (0.1 mg/kg) in saline for pain management. Viruses were allowed to express for 3–4 weeks before imaging was performed.

Neonatal viral injection

Intraventricular viral injections were carried out in C57Bl/6N (Charles River Labs) neonates[37]. Briefly, postnatal day 1 (P1) pups were anesthetized by placing them on an aluminum plate resting on ice. A Kimwipe was used to prevent direct contact of the pup with the cold plate. When the pup was no longer responsive to toe pinch, it was moved onto the stereotaxic apparatus while maintained cold. Injections were targeted to the right lateral ventricle (approximate coordinates in mm from Lambda: AP +1.4, ML +0.8, DV −1.5). 1 μL of solution containing a total of 2.0×10^9 g.c. of Voltron2-ST virus and 1.0×10^9 g.c. of Cre virus in sterile PBS was injected slowly into the ventricle. For optogenetic experiments,

3.0×10^9 g.c. of AAV8-Syn-ChR2(H134R)-GFP-WPRE (Addgene #58880-AAV8) virus was also included in the injection solution. To visualize successful delivery of virus, 0.05% Trypan blue was added to the injected solution. Pups were allowed to recover on a 37°C warming pad before being returned into the cage with the dam. The behavior of the dam was carefully monitored for 2 hours following injections to ensure maternal care of the pups.

In vitro imaging and electrophysiology

Acute slice preparation was carried out using protocols optimized for adult tissue[38]. Briefly, animals were perfused with 15 mL chilled and carbogen-bubbled (5% CO_2/95% O_2) NMDG aCSF (in mM: 92 NMDG, 2.5 KCl, 1.25 NaH_2PO_4, 30 $NaHCO_3$, 20 HEPES, 25 glucose, 2 thiourea, 5 Na-ascorbate, 3 Na-pyruvate, 0.5 $CaCl_2{\cdot}4H_2O$ and 10 $MgSO_4{\cdot}7H_2O$, pH 7.3–7.4, 300–310 mOsm) at a rate of 10 ml/min via manual cardiac perfusion. Brain tissues were quickly dissected and sliced to 300 μm using a vibratome (Precisionary Instruments) in chilled/bubbled NMDG aCSF. Following Na+ spike-in in 37°C NMDG aCSF, slices were placed in room-temperature HEPES aCSF (in mM: 92 NaCl, 2.5 KCl, 1.25 NaH_2PO_4, 30 $NaHCO_3$, 20 HEPES, 25 glucose, 2 thiourea, 5 Na-ascorbate, 3 Na-pyruvate, 2 $CaCl_2{\cdot}4H_2O$ and 2 $MgSO_4{\cdot}7H_2O$, pH 7.3–7.4, 300–310 mOSm) containing 25 nmol of JF585[8,39] and incubated for 1 hour in the dark. Slices were then moved to HEPES aCSF for 1 hr to washout excess dye before imaging. *In vitro* slices were imaged while perfusing bubbled, room temperature HEPES aCSF. Whole-cell recordings were made using filamented glass pipettes (Sutter #BF150-86-10) pulled to 3–8 MOhm resistance (Sutter P-1000 Micropipette Puller), and intracellular recording buffer containing (in mM) 145 K-Gluconate, 10 HEPES, 1 EGTA, 2 Mg-ATP, 0.3 Na_2-GTP, and 2 $MgCl_2$ (pH 7.3, 290–300 mOsm). A patch-clamp headstage (Molecular Devices #1-CV-7B) mounted on a motorized 4-axis Siskiyou MX7600 manipulator, and Axon Instruments MultiClamp 700b amplifier were used for all recordings.

In vivo cranial window implant and labeling

Adult mice that received Voltron2-ST injections as neonates (see above) were used for *in vivo* imaging experiments. At 5–6 weeks, a 2.5 mm-diameter craniotomy was made above the motor cortex. Cranial windows were fabricated by stacking two 2.5 mm coverglass discs (#1.5 glass, Potomac) and one 3.5 mm disc (#1.5 glass, Potomac) and secured them together with optical glue. These glass windows were implanted into the craniotomy and affixed to the skull with super glue. A headbar was then affixed caudal to the window. Dental acrylic (Jet repair; Pearson Dental) was used to secure the headbar to the skull and protect exposed bone. 24 hours prior to imaging, a retroorbital injection was performed to deliver 100 μL of solution containing 20 μL of Pluronic F-127 (20% w/v), 20 μL of DMSO, and 100 nmol of JF552 dye in sterile PBS.

Microprism implant

The surgical procedure to implant the glass microprism into cortex was performed similarly to cranial window implant protocols detailed in Kılıç et al.[40]. Briefly, the animal was anesthetized and given pre-operative cefazolin and buprenorphine for pain management. The depilated scalp was resected to expose the entirety of the dorsal skull. A headbar was attached to the skull approximately over the lambda suture using cyanoacrylate glue (Loctite 4014) and dental acrylic, and the skin margins were secured to the outer edges

of the skull using glue. A 3.5 mm diameter craniotomy was made over sensory cortex to accommodate the microprism assembly. A small lip was carved into the skull to allow the assembly coverglass to sit flush with the skull surface while resting on a thin layer of bone. The assembly was made by gluing a 1.0 mm glass microprism (hypotenuse coated with enhanced aluminum; Tower Optical) to a 3.5 mm-diameter round coverglass using optical glue (Norland NOA61). Before implanting the assembly, 100 nL of AAV1-hSyn-FLEX-Voltron2-ST-WPRE mixed with 1:50 retroAAV-hSyn-Cre was injected into 3 sites across the craniotomy, at −200 μm and −500 μm depths at each injection site. Virus was allowed to settle for approximately 15 minutes after each injection. A straight-line incision into the cortex was made using a micro scalpel blade mounted to the stereotaxic manipulator. The scalpel was inserted into the cortex first to a depth of −200 μm, and then translated in a straight line across ~1.0 mm of cortex. The scalpel was removed and then reinserted at the start position of the incision to a depth of −400 μm and the 1.0 mm incision was made again. This process was repeated at −750 μm and −1000 μm. The assembly was then positioned by slowly pressing the microprism edge into the incised cortex until the coverglass sat flush with the skull surface. A plastic pipette tip was attached to the stereotaxic manipulator and used to maintain downward pressure on the assembly while the brain tissue settled around the implanted prism. The edges of the coverglass were secured to the skull using cyanoacrylate glue, and the entire skull cap was then covered with dental acrylic while ensuring that the coverglass remained exposed. Animals were given post-operative buprenorphine and ketoprofen for 2 days following the surgery and carefully monitored for 3 days after the procedure to ensure full recovery. Imaging was performed 3–5 weeks following implantation but imaging at later time points was not prohibited by changes in implant quality.

Image processing and analysis

All data were analyzed using custom scripts written in MATLAB (Mathworks). Binary regions of interest (ROIs) spanning all four planes were determined semi-automatically[1,41] using the average images measured across all even (forward scan) frames. ROIs determined from even frames were warped onto odd frames (reverse scan frames) using an affine transform computed using a similarity-based metric applied to averages of odd and even frames to correct for small differences induced by bidirectional scanning. ROIs were not constrained to be spatially contiguous. The fluorescence time series corresponding to each ROI was computed as the summed intensity over all pixels included within the ROI. In all analyses, dF/F was calculated as $(F-F_0)/F_0$, where F_0 was taken to be the mean fluorescence. The relationship between dF/F measurements and voltage measurements were determined with least squares fits (Fig. 2c,d). To calculate F_0 in units of photons/cell/frame as reported in Fig. 4b and Supplementary Table 2, we needed the scaling factor relating the number of detected photons to the output of our digitizer (ADU). This is given by

$$\frac{\text{ADU}}{\text{detected photon}} = \frac{qG_DG_A2^B}{T\Delta V} = 190$$

where q = electron charge (1.6×10^{-19} C); G_D = SiPM detector charge gain (5×10^6); G_A = transimpedance amplifier gain (500 V/A); B = digitizer bit depth (16); T = pixel period

(66.67 ns); ΔV = digitizer input voltage range (2.085 V). This scaling factor was further verified using an analysis of the signal variance across images.

In Fig. 4b, to account for cells spanning multiple planes, cell depth was computed as the average depth based on the number of ROI pixels in each plane. We estimated the background level by measuring fluorescence intensity in a manually selected ROI located adjacent to the cell. Background ROIs included approximately the same number of pixels per plane as cell ROIs and avoided Voltron-labeled cells. Average photon counts per frame for cell and background ROIs, $\langle F_{cell} \rangle$ and $\langle F_{bg} \rangle$, were computed from the first 256 frames of each acquisition. To account for any difference in pixels between cell and background ROI, $\langle F_{bg} \rangle$ was adjusted with a scaling factor related to ROI size, yielding $\langle F_{bg} \rangle'$, an estimate for the background component in each cell ROI measurement. Contrast, K was calculated as $(\langle F_{cell} \rangle - \langle F_{bg} \rangle')/\langle F_{cell} \rangle$. Because not all cells demonstrated spiking behavior during imaging, we calculated an "estimated spike SNR", $(dF/F)K\sqrt{\langle F_{cell} \rangle}$ where signal is calculated as a 10% change in signal but not background (i.e. $10\% \times K$) due to an action potential. The horizontal line drawn at Spike SNR = 3.5 indicates the SNR required for a spike detection performance of about 75% precision and 75% recall (10 Hz spiking rate, discriminator set to 80% of the average spike amplitude). Photobleaching rate was estimated from a first order exponential fit to the entire acquisition time series. Dashed lines in Fig. 4b represent single exponential fits, with the exception of the fit to contrast, which was linear. Data was tabulated in Microsoft Office Excel 2019.

In Fig. 6d,e, single action potentials (measured both electrically and optically) were peak-aligned in time prior to averaging. In Fig. 2d, repeated measurements (using subthreshold and suprathreshold current steps) were made in some cells. In some experiments, a modest amount of photobleaching (typically less than 20%, EDFig. 3) was corrected for with a high-pass 2nd order Butterworth filter with a cutoff frequency of 0.5 Hz. Traces were low pass-filtered using causal boxcar filters. Lateral motion correction was applied to image stacks recorded in vivo. Displacements in the x- and y-directions were determined using cross-correlation at subpixel resolution. Displacements were calculated separately for each image plane and the mean displacement applied uniformly to all planes. For measurements of background-to-signal ratio for sparse *in vivo* labeling (reported in Results) were calculated based on images in reference [8]. Somata locations were identified manually, and fluorescence was taken as the median pixel value within a 7.5-pixel radius around those locations. Background fluorescence was taken as the median fluorescence across four same-sized ROIs displaced to the left, to the right, above, and below the soma center by 50 pixels.

PSF simulations

To estimate the collection efficiency and effect of cranial window-induced aberrations, we developed a wave-based numerical model for the MuZIC point spread function (PSF). We computed the illumination and detection 3D PSFs separately, taking into account upstream pinhole occlusion (see Supplementary Note 5 for additional details). The illumination and detection PSFs are pair-wise multiplied to yield the final confocal PSFs.

Statistics and Reproducibility

All data reported in the manuscript were reproduced across multiple fields of view, days, and mice as indicated. Summary statistics are descriptive in nature and no statistical tests are performed. For this reason, this study did not include any randomization or blinding and sample sizes were not pre-determined. No data points were excluded.

Extended Data

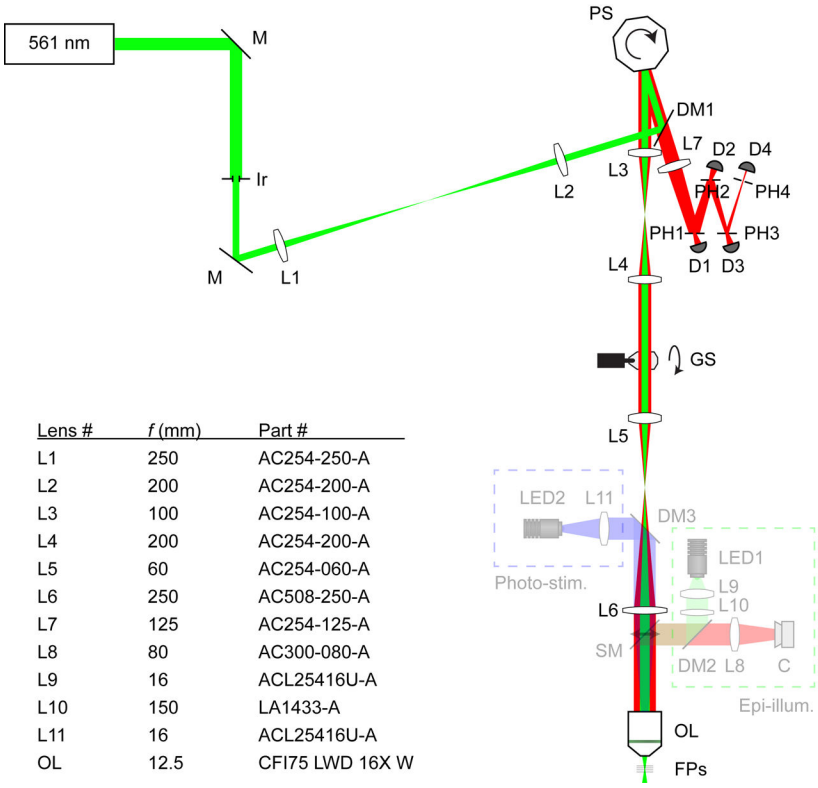

Lens #	*f* (mm)	Part #
L1	250	AC254-250-A
L2	200	AC254-200-A
L3	100	AC254-100-A
L4	200	AC254-200-A
L5	60	AC254-060-A
L6	250	AC508-250-A
L7	125	AC254-125-A
L8	80	AC300-080-A
L9	16	ACL25416U-A
L10	150	LA1433-A
L11	16	ACL25416U-A
OL	12.5	CFI75 LWD 16X W

Element Pair	Distance (mm)
Ir - L1	250
L1 - L2	441
L2 - DM1	128
DM1 - PS	72
PS - L3	98
L3 - L4	292
L4 - GS	201
GS - L5	60
L5 - L6	299
L6 - OL shoulder	201
PS - L7	124
L7 - PH1	61
PH1 - D1	50
PH1 - PH2	60

Extended Data Fig. 1 - Detailed system schematic.

The light source is a continuous-wave laser diode (“561 nm”). Blue dashed box (“Photo-stim.”) denotes components of the full-field photo-stimulation module. Green dashed box (“Epi-illum.”) denotes components of the epi-illumination widefield fluorescence microscopy unit. M: mirror, Ir: iris, L: lens, DM: dichroic mirror, PS: polygonal scanner, GS: galvanometer scanner, SM: switchable mirror, OL: objective lens, FPs: focal planes, PH: pinhole, D: detector, C: camera. All part numbers are for the manufacturer Thorlabs, except the objective lens (Nikon).

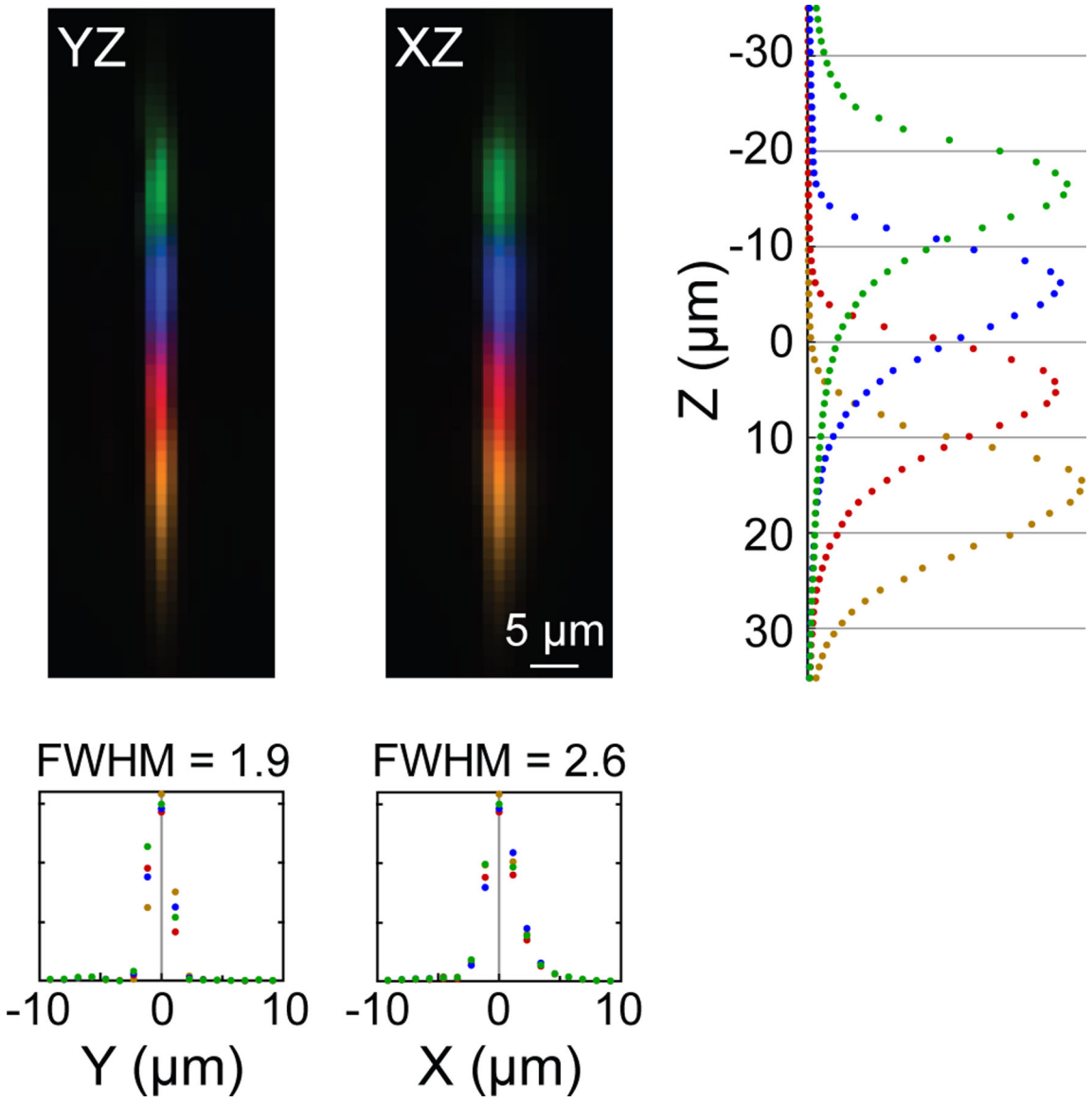

Extended Data Fig. 2 - System resolution.

Experimental measurements of the combined excitation and emission point spread functions (PSFs)corresponding to the four simultaneously acquired image planes. Confocal pinhole diameters were selected so that PSFs corresponding to adjacent detectors overlap, eliminating gaps between the four imaging planes, which together cover ~40 µm in the axial direction. Lateral resolution was somewhat anisotropic on account of the slower detector fall time. (X: 2.6 µm full-width half-max; Y: 1.9 µm).

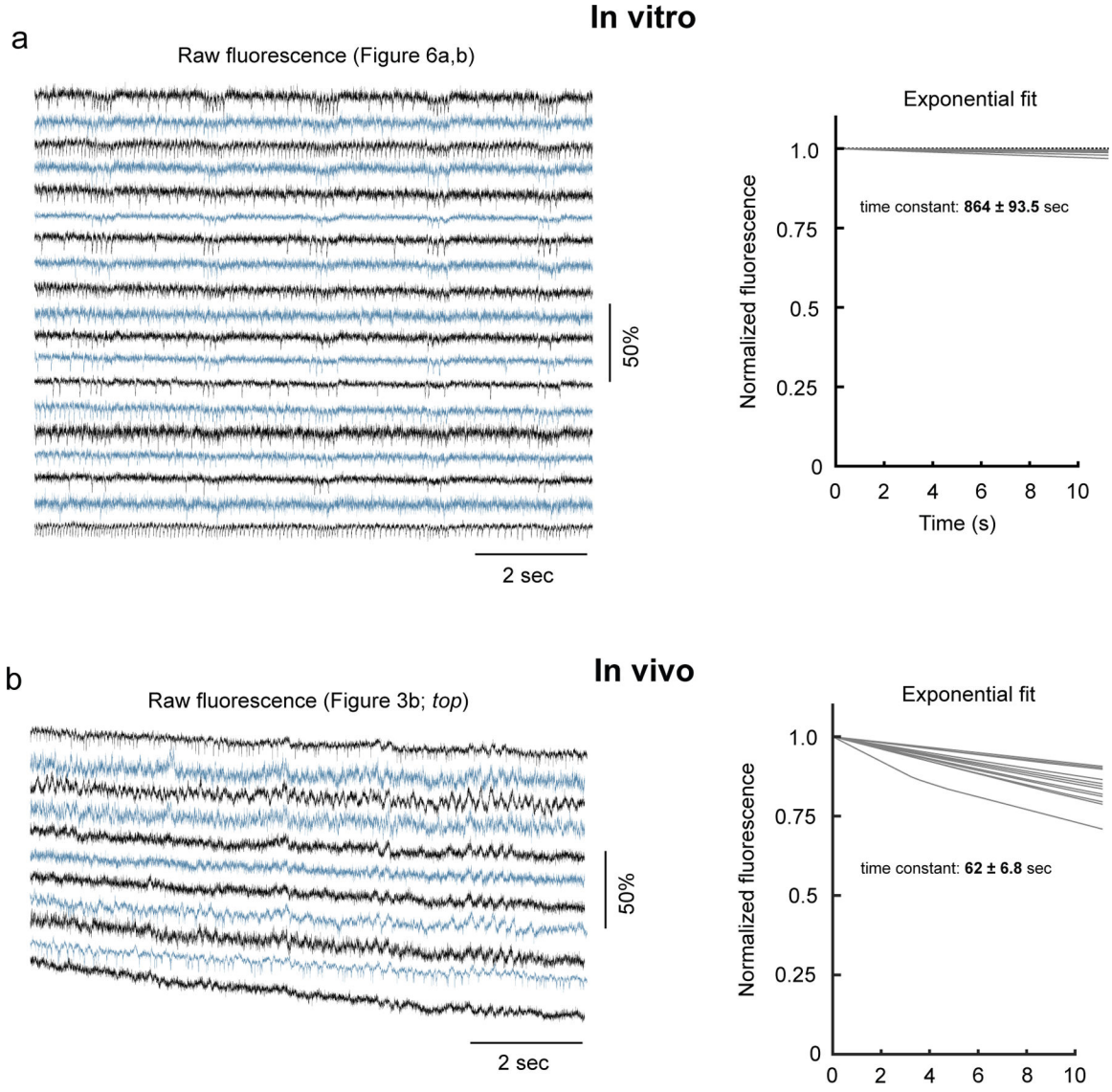

Extended Data Fig. 3- Photobleaching.

a. *Left*, Example of raw, unprocessed fluorescence from all cells identified from the in vitro imaging experiment depicted in Fig. 6a,b. *Right*, Exponential fits to raw fluorescence normalized to initial brightness. These data were collected with the highest excitation power of all in vitro experiments (561 nm; 23.6 mW/mm2). **b.** Raw, unprocessed recorded from all cells identified in the in vivo imaging experiment depicted in Fig. 3b (*top*) and exponential fits to in vivo fluorescence, as in (a). The same excitation power was used for all in vivo imaging experiments (561 nm; 300 mW/mm2).

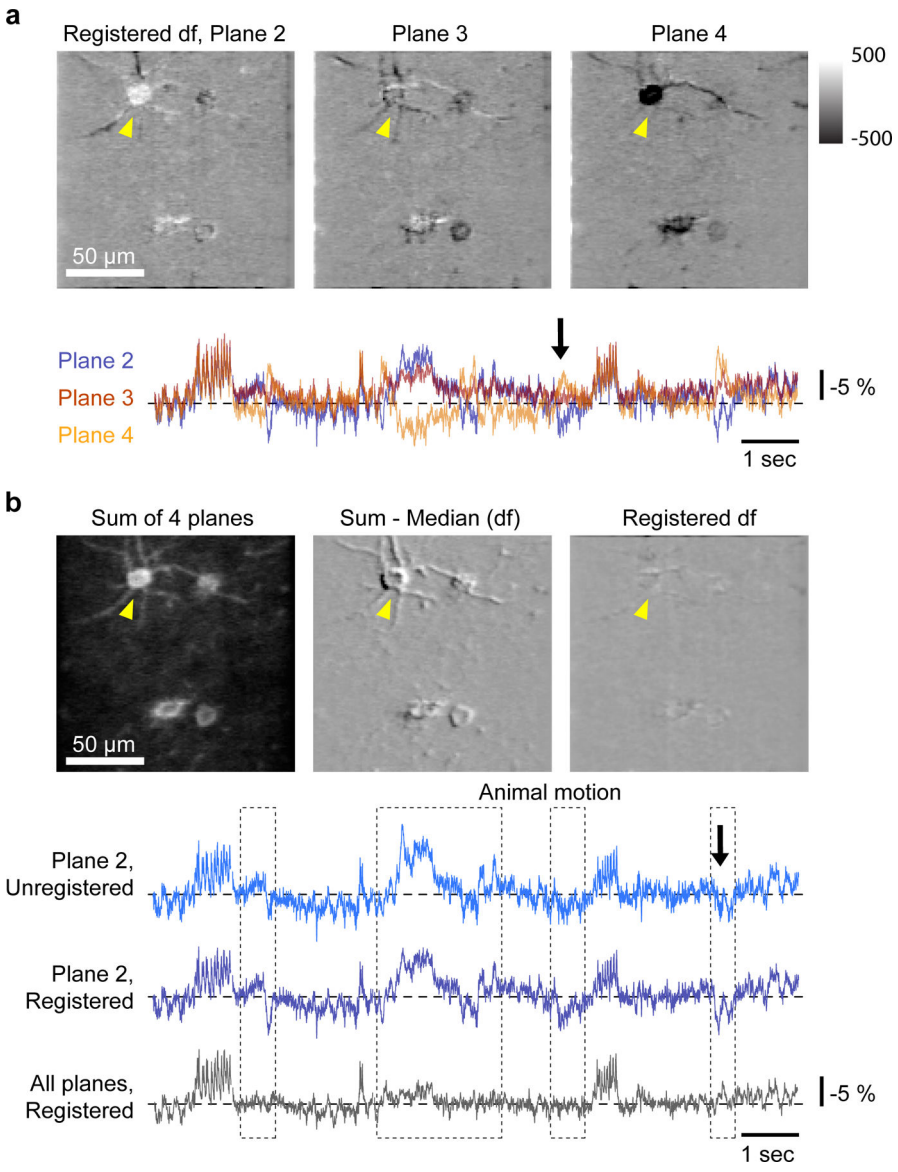

Extended Data Fig. 4 - Multi-Z imaging minimizes axial motion artifacts.

a. During periods of brain motion, fluorescence is redistributed across planes, with cells becoming brighter in some planes and dimmer in others. *Top*, average change in fluorescence during a period of movement indicated by arrow below in adjacent planes. *Bottom*, average fluorescence time series corresponding to the cell indicated (yellow arrowhead). **b.** *Top*, mean fluorescence (*left*), difference image prior to (*middle*) and following (right)lateral motion correction. Sum of 4 image planes shown. During periods of brain motion (indicated by black arrow, *bottom*), lateral motion correction compensates for brain motion. *Bottom*, fluorescence time series corresponding to the cell indicated (yellow arrowhead, *top*). Time series extracted from a single plane (plane 2) before lateral motion correction (light blue, *top*), after lateral motion correction (dark blue, *middle*), and from a region of interest (ROI) spanning all four image planes following lateral motion correction (gray, *bottom*). Artifacts introduced by brain motion are suppressed when extracting time

series from multiplane ROIs. Data are representative of axial motion across 34 fields, 5 animals.

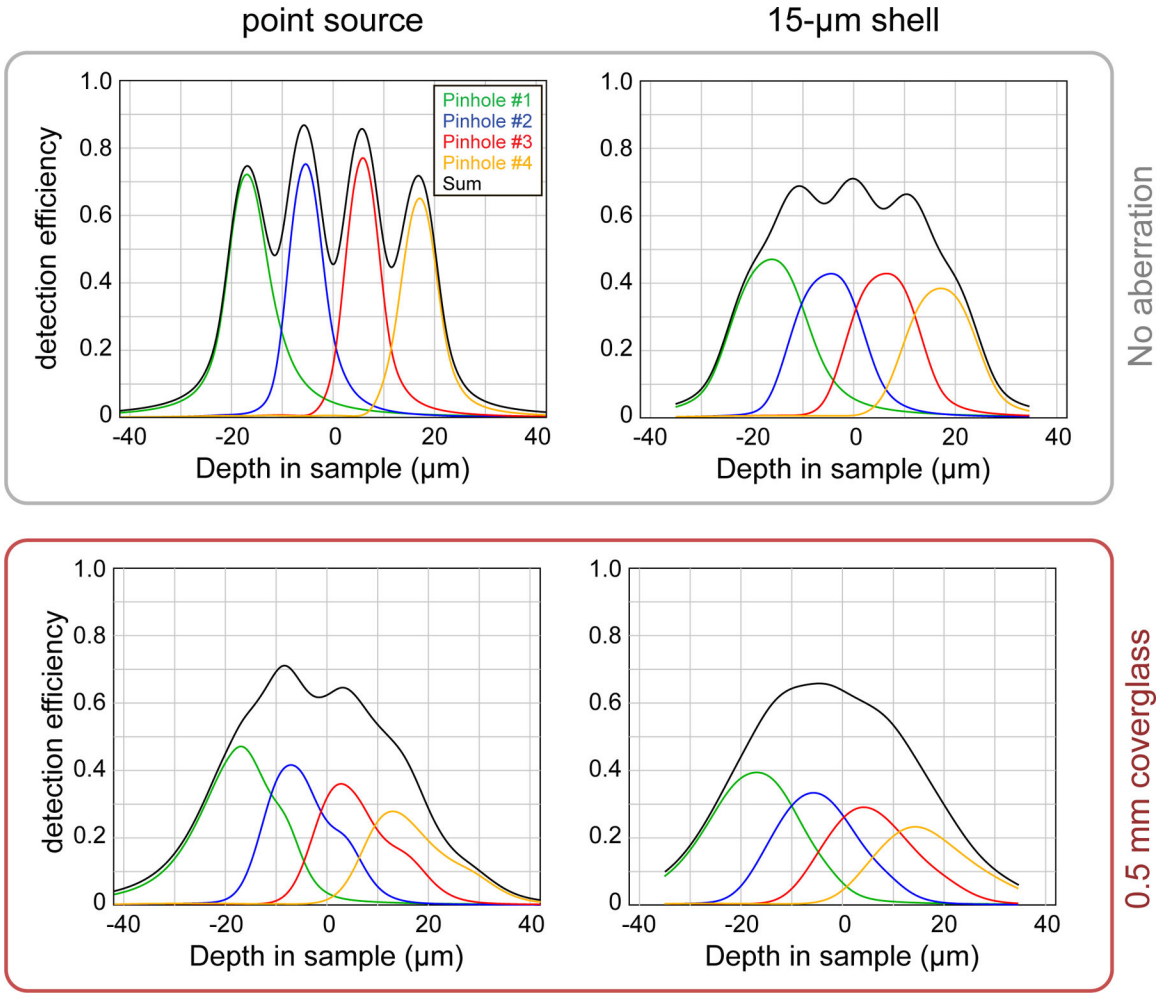

Extended Data Fig. 5 - Confocal collection efficiency.

Simulated confocal collection efficiency for fluorescence emitted from point sources (*left*) and 15-µm shells (*right*) located at different axial positions. Axial resolution is degraded as a result of spherical aberration induced by imaging through 0.5 mm cover glass (bottom; RI = 1.52). Lateral resolution is not degraded as much as axial resolution, meaning that the total fluorescence together collected by all detectors is only modestly reduced. See Methods and Supplementary Note 4 for more details.

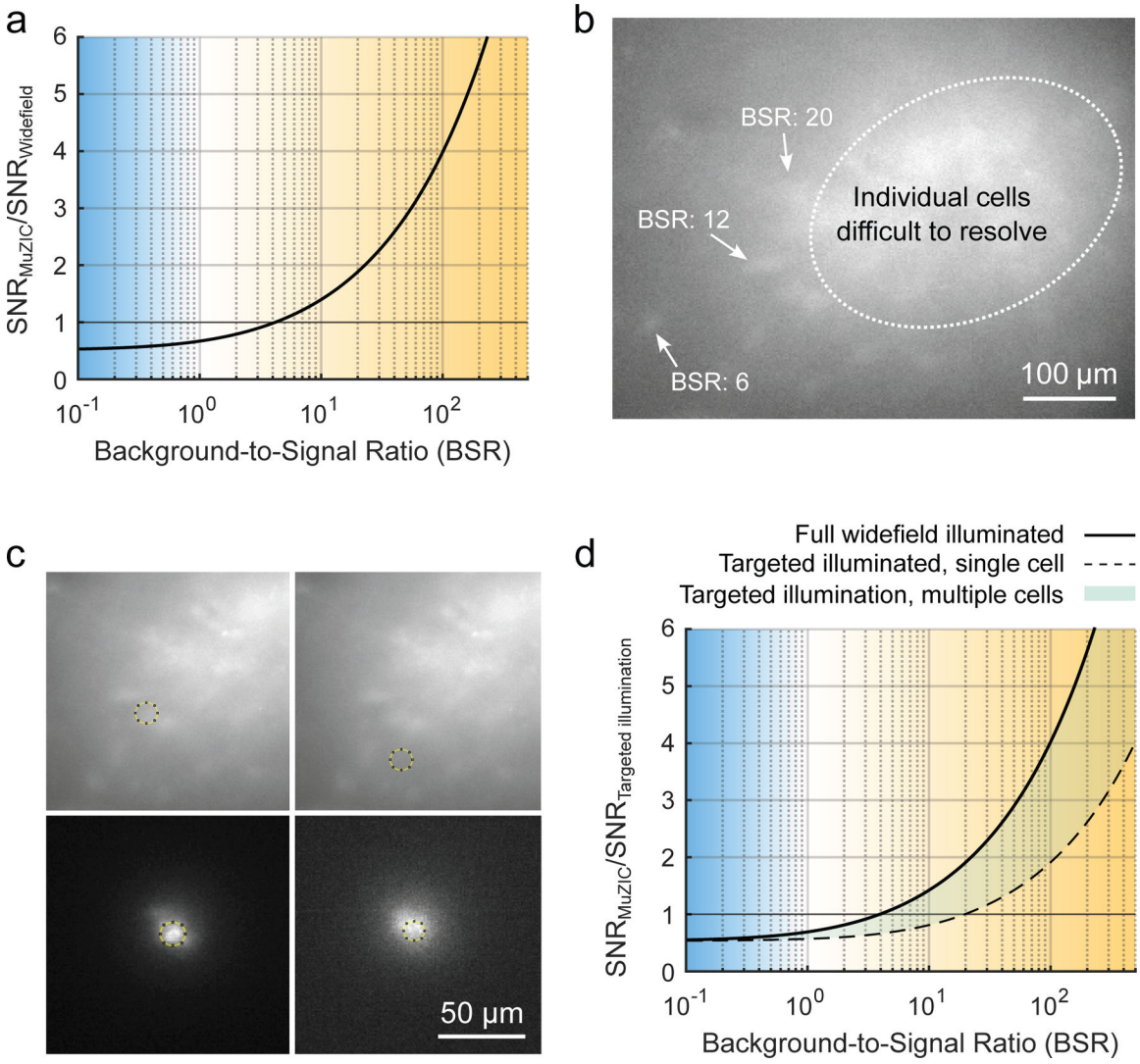

Extended Data Fig. 6 - Comparison of MuZIC and widefield fluorescence microscopy (WFM).

a. Signal-to-noise ratio of MuZIC relative to WFM increases with increasing WFM background-to-signal ratio (BSR). SNR of MuZIC is mostly insensitive to out-of-focus background fluorescence, while SNR of WFM decreases with increasing background. When BSR is greater than about 5, SNR of MuZIC is higher than SNR of WFM (assuming contrast of MuZIC is 0.6 and detection efficiency of MuZIC is 25% relative to WFM; see Supplementary Note 2). **b.** WFM image of Voltron2-labeled neurons in vivo. Representative BSRs associated with different neurons are indicated for reference. Individual neurons were difficult to resolve in regions of higher labeling density (representative of 4 animals). **c.** Example in-vivo widefield images of neurons without (*top*) and with (*bottom*) targeted illumination delimited by dashed circles. Dashed circles span regions of interest encompassing a single neuron (*top left*: signal + background) and background only (*top right*). Corresponding images when targeted illumination was applied (*bottom*) are shown recentered. In this extreme example where only a single neuron is targeted, the BSR is found to be reduced by a factor $\gamma = 0.2$ (see Supplementary Note 3, representative of 4 animals).

d. Signal-to-noise ratio of MuZIC relative to WFM without (*solid*) and with (*dashed*) the addition of targeted illumination of a single neuron (i.e. $\gamma = 0.2$). In general, when multiple neurons are targeted, the reduction in BSR is not as significant and the relative SNR gain provided by MuZIC lies within the shaded region. Targeted illumination has the effect of shifting the break-even point where MuZIC becomes advantageous over WFM to a higher BSR value, up to about 25 in the very extreme case of single-neuron targeted illumination.

Supplementary Material

Refer to Web version on PubMed Central for supplementary material.

ACKNOWLEDGMENTS

The authors thank Ahmed Abdelfattah, Amrita Singh, Gabe Murphy and Karel Svoboda for technical advice and helpful discussions. The authors thank Eric Schreiter and Ilya Kolb for sharing Voltron2-ST reagents pre-publication. The authors thank Michael Giacomelli for advice on silicon photomultipliers. We thank Tim Wang and David Kleinfeld for helpful comments on the manuscript. This work was supported by research grants from the National Institutes of Health: R01EB029171 (J.M.), RF1MH126882 (M.N.E.), and F32MH129149 (M.V.M). The funder had no role in study design, data collection and analysis, decision to publish or preparation of the manuscript.

DATA AVAILABILITY

Data described in this study are available on Figshare (DOI: 10.6084/m9.figshare.23542167). Information describing construction of our MuZIC system is available via Github (detector: https://github.com/tweber225/simple-sipm; assembly: https://github.com/tweber225/muzic).

REFERENCES

1. Chen T-W et al. Ultrasensitive fluorescent proteins for imaging neuronal activity. Nature 499, 295–300 (2013). [PubMed: 23868258]
2. Tian L et al. Imaging neural activity in worms, flies and mice with improved GCaMP calcium indicators. Nat. Methods 6, 875–881 (2009). [PubMed: 19898485]
3. Zhang Y et al. Fast and sensitive GCaMP calcium indicators for imaging neural populations. Nature 615, 884–891 (2023). [PubMed: 36922596]
4. Grienberger C & Konnerth A Imaging calcium in neurons. Neuron 73, 862–885 (2012). [PubMed: 22405199]
5. Luo L, Callaway EM & Svoboda K Genetic dissection of neural circuits: a decade of progress. Neuron 98, 256–281 (2018). [PubMed: 29673479]
6. Wachowiak M et al. Optical dissection of odor information processing in vivo using GCaMPs expressed in specified cell types of the olfactory bulb. J. Neurosci 33, 5285–5300 (2013). [PubMed: 23516293]
7. Wei Z et al. A comparison of neuronal population dynamics measured with calcium imaging and electrophysiology. PLOS Comput. Biol 16, e1008198 (2020). [PubMed: 32931495]
8. Abdelfattah AS et al. Bright and photostable chemigenetic indicators for extended in vivo voltage imaging. Science 365, 699–704 (2019). [PubMed: 31371562]
9. Abdelfattah AS et al. Sensitivity optimization of a rhodopsin-based fluorescent voltage indicator. Neuron 111, 1547–1563 (2023). [PubMed: 37015225]
10. Piatkevich KD et al. Population imaging of neural activity in awake behaving mice. Nature 574, 413–417 (2019). [PubMed: 31597963]

11. Adam Y et al. Voltage imaging and optogenetics reveal behaviour-dependent changes in hippocampal dynamics. Nature 569, 413–417 (2019). [PubMed: 31043747]
12. Villette V et al. Ultrafast two-photon imaging of a high-gain voltage indicator in awake behaving mice. Cell 179, 1590–1608 (2019). [PubMed: 31835034]
13. Hochbaum DR et al. All-optical electrophysiology in mammalian neurons using engineered microbial rhodopsins. Nat. Methods 11, 825–833 (2014). [PubMed: 24952910]
14. Knöpfel T, Gallero-Salas Y & Song C Genetically encoded voltage indicators for large scale cortical imaging come of age. Curr. Opin. Chem. Biol 27, 75–83 (2015). [PubMed: 26115448]
15. Xiao S et al. Large-scale voltage imaging in behaving mice using targeted illumination. iScience 24, 103263 (2021). [PubMed: 34761183]
16. Kazemipour A et al. Kilohertz frame-rate two-photon tomography. Nat. Methods 16, 778–786 (2019). [PubMed: 31363222]
17. Wu J et al. Kilohertz two-photon fluorescence microscopy imaging of neural activity in vivo. Nat. Methods 17, 287–290 (2020). [PubMed: 32123392]
18. Piatkevich KD et al. A robotic multidimensional directed evolution approach applied to fluorescent voltage reporters. Nat. Chem. Biol 14, 352–360 (2018). [PubMed: 29483642]
19. Brinks D, Klein AJ & Cohen AE Two-photon lifetime imaging of voltage indicating proteins as a probe of absolute membrane voltage. Biophys. J 109, 914–921 (2015). [PubMed: 26331249]
20. Chamberland S et al. Fast two-photon imaging of subcellular voltage dynamics in neuronal tissue with genetically encoded indicators. eLife 6, e25690 (2017). [PubMed: 28749338]
21. Badon A et al. Video-rate large-scale imaging with multi-Z confocal microscopy. Optica 6, 389–395 (2019). [PubMed: 34504902]
22. Tsang J-M et al. Fast, multiplane line-scan confocal microscopy using axially distributed slits. Biomed. Opt. Express 12, 1339–1350 (2021). [PubMed: 33796357]
23. Lillis KP, Eng A, White JA & Mertz J Two-photon imaging of spatially extended neuronal network dynamics with high temporal resolution. J. Neurosci. Methods 172, 178–184 (2008). [PubMed: 18539336]
24. Göbel W, Kampa BM & Helmchen F Imaging cellular network dynamics in three dimensions using fast 3D laser scanning. Nat. Methods 4, 73–79 (2007). [PubMed: 17143280]
25. Katona G et al. Fast two-photon in vivo imaging with three-dimensional random-access scanning in large tissue volumes. Nat. Methods 9, 201–208 (2012). [PubMed: 22231641]
26. Grewe BF, Langer D, Kasper H, Kampa BM & Helmchen F High-speed in vivo calcium imaging reveals neuronal network activity with near-millisecond precision. Nat. Methods 7, 399–405 (2010). [PubMed: 20400966]
27. Nadella KMNS et al. Random-access scanning microscopy for 3D imaging in awake behaving animals. Nat. Methods 13, 1001–1004 (2016). [PubMed: 27749836]
28. Lakowicz JR Principles of fluorescence spectroscopy (Springer, 2006).
29. Andermann ML et al. Chronic cellular imaging of entire cortical columns in awake mice using microprisms. Neuron 80, 900–913 (2013). [PubMed: 24139817]
30. Rickgauer JP, Deisseroth K & Tank DW Simultaneous cellular-resolution optical perturbation and imaging of place cell firing fields. Nat. Neurosci 17, 1816–1824 (2014). [PubMed: 25402854]
31. Packer AM, Russell LE, Dalgleish HWP & Häusser M Simultaneous all-optical manipulation and recording of neural circuit activity with cellular resolution in vivo. Nat. Methods 12, 140–146 (2015). [PubMed: 25532138]
32. Altkorn R & Zare RN Effects of saturation on laser-induced fluorescence measurements of population and polarization. Annu. Rev. Phys. Chem 35, 265–289 (1984).
33. Zhang L et al. Miniscope GRIN lens system for calcium imaging of neuronal activity from deep brain structures in behaving animals. Curr. Protoc. Neurosci 86, e56 (2019). [PubMed: 30315730]
34. Murayama M & Larkum ME In vivo dendritic calcium imaging with a fiberoptic periscope system. Nat. Protoc 4, 1551–1559 (2009). [PubMed: 19798087]

METHODS-ONLY REFERENCES

35. Pologruto TA, Sabatini BL, & Svoboda K ScanImage: flexible software for operating laser scanning microscopes. Biomed. Eng. Online 2, 13 (2003). [PubMed: 12801419]
36. Savarese M et al. Fluorescence lifetimes and quantum yields of rhodamine derivatives: new insights from theory and experiment. J. Phys. Chem. A 116, 7491–7497 (2012). [PubMed: 22667332]
37. Kim J-Y, Grunke SD, Levites Y, Golde TE & Jankowsky JL Intracerebroventricular viral injection of the neonatal mouse brain for persistent and widespread neuronal transduction. JoVE, e51863 (2014).
38. Ting JT, Daigle TL, Chen Q & Feng G Acute Brain Slice Methods for Adult and Aging Animals: Application of Targeted Patch Clamp Analysis and Optogenetics. in Patch-Clamp Methods and Protocols (eds. Martina M & Taverna S) 221–242 (Springer New York, 2014).
39. Grimm JB et al. A general method to fine-tune fluorophores for live-cell and in vivo imaging. Nat. Methods 14, 987–994 (2017). [PubMed: 28869757]
40. Kılıç K et al. Chronic cranial windows for long term multimodal neurovascular imaging in mice. Front. Physiol 11, 612678 (2021). [PubMed: 33551837]
41. Peron SP, Freeman J, Iyer V, Guo C & Svoboda K A cellular resolution map of barrel cortex activity during tactile behavior. Neuron 86, 783–799 (2015). [PubMed: 25913859]

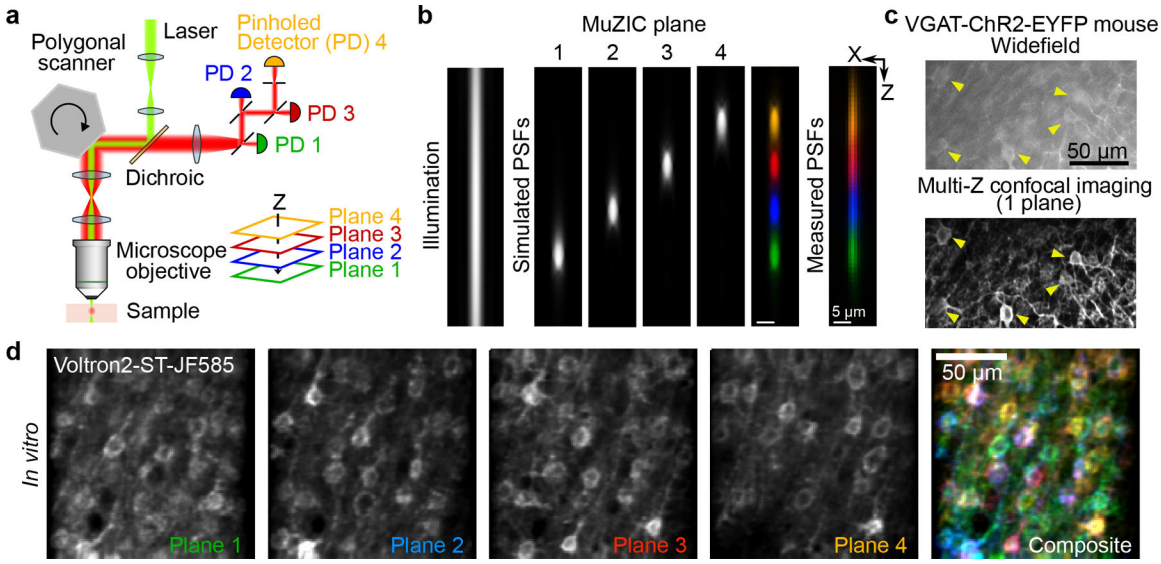

Figure 1 –. High-contrast multiplane imaging in densely labeled tissue with MuZIC.

a. Schematic of optical system. High speed scanning is achieved with a 128-facet polygonal scanner operating at 54,945 RPM. Excitation light (*green*) underfills the objective creating an axially extended illumination beam. Fluorescence is collected through a series of axially distributed reflective pinholes which map to different planes in the sample. **b.** Numerical simulation of illumination beam (*left*), simulated point spread functions (PSFs) associated with each image plane (*middle, colors*), and corresponding PSFs measured experimentally (*right,* representative of 10 measurements). **c.** Membrane-bound YFP in a fixed section from a VGAT-ChR2-YFP mouse visualized with MuZIC and widefield microscopy to demonstrate optical sectioning. Confocal pinholes reject background fluorescence while preserving in-plane signal (representative of 20 fields). **d.** Neurons densely labeled with Voltron2-ST_{JF585} can be simultaneously visualized across four focal planes (representative of 40 fields).

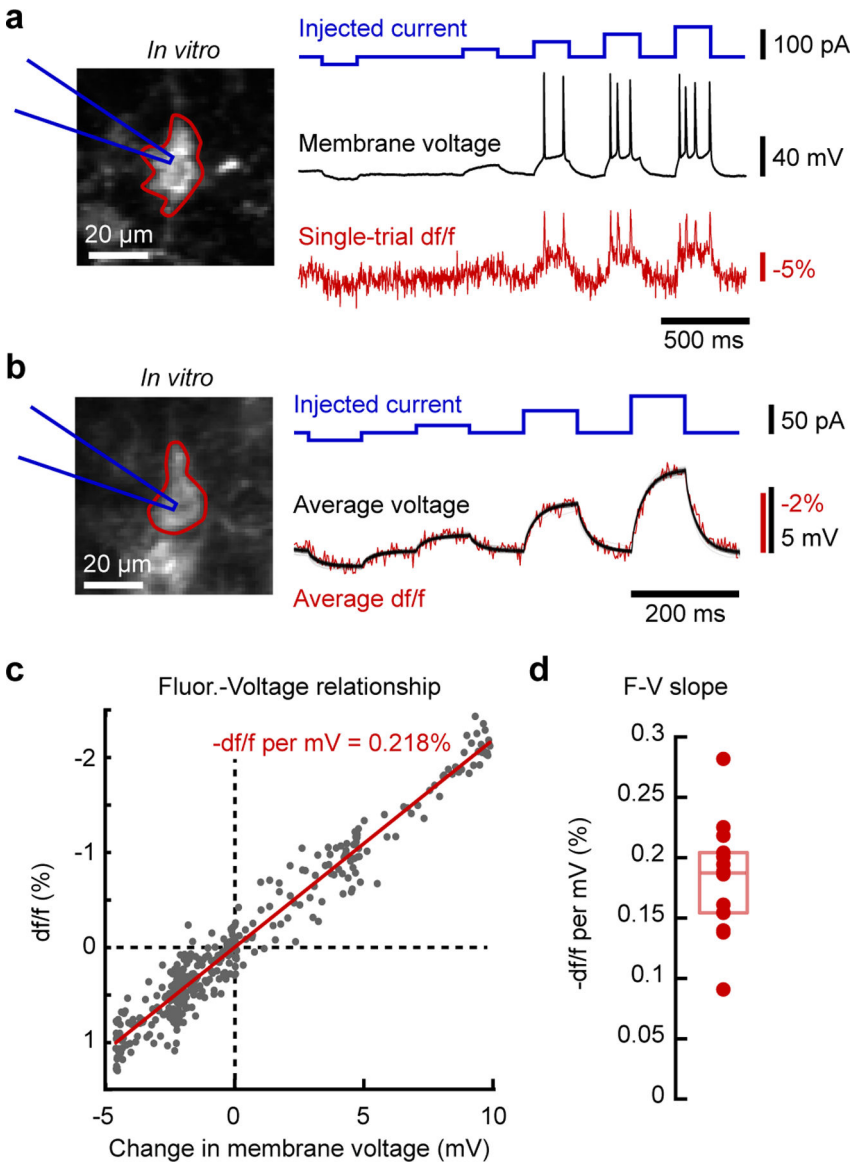

Figure 2 –. MuZIC enables high-SNR GEVI imaging in vitro.

a. Simultaneous whole-cell patch-clamp recording and voltage imaging in a cortical pyramidal neuron *in vitro*. Subthreshold membrane potential dynamics and action potentials can be detected optically in single-trial measurements from the region of interest (ROI) outlined in red (representative of 8 cells, 3 animals). **b.** Averaging across trials (100 repetitions) reduces shot noise to reveal millivolt-scale dynamics, which are reported on a linear scale (**c**) (representative of 14 cells, 3 animals). **d**. The relationship between changes in fluorescence and membrane potential was similar across recorded neurons (n=14 cells, 3 animals; box plot displays median and interquartile intervals).

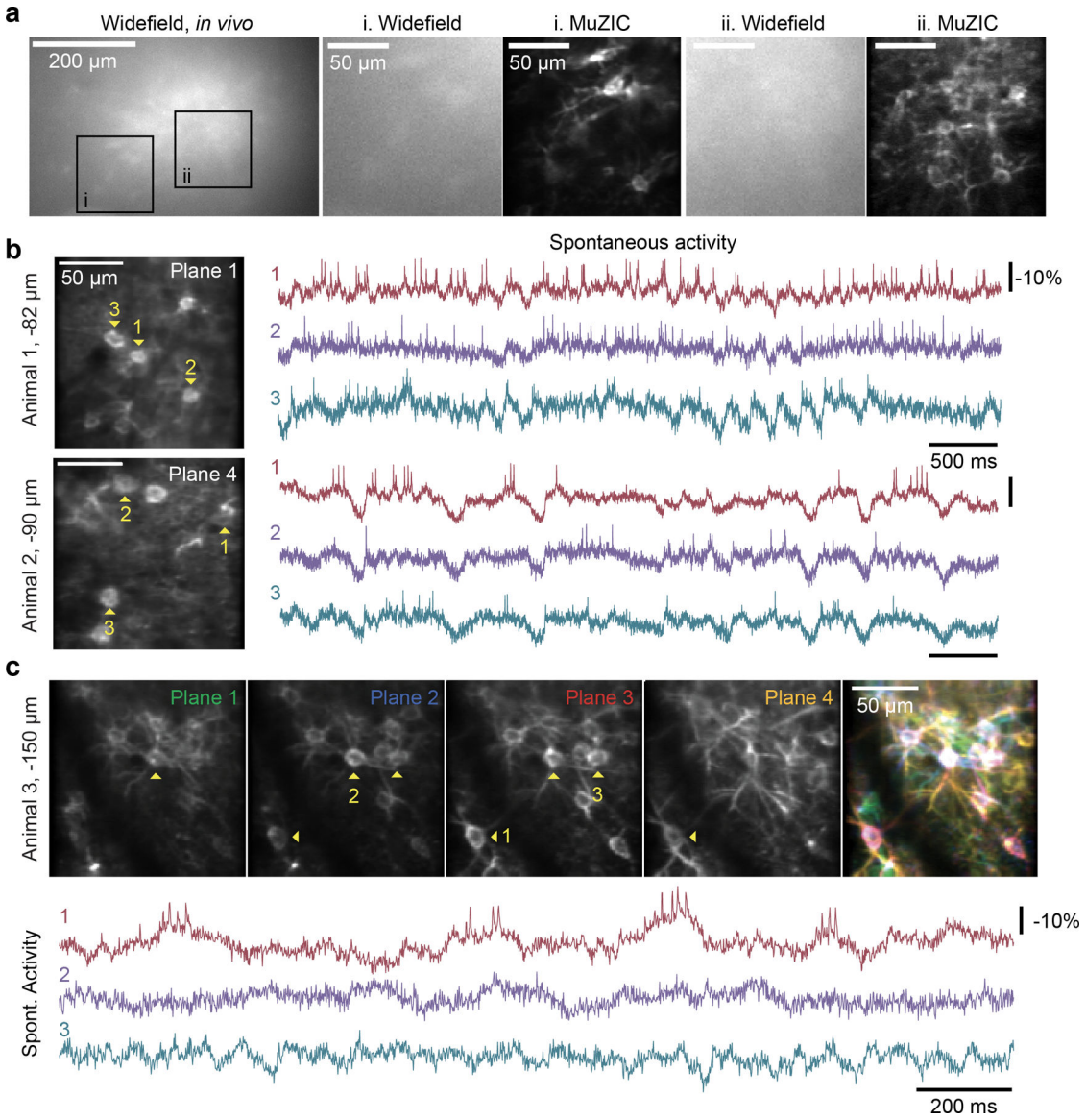

Figure 3 –. MuZIC reports subthreshold and suprathreshold activity in neural ensembles in vivo.

a. Widefield image of neurons labeled with Voltron2-ST$_{JF552}$ *in vivo* (*far left*). Insets highlight two FOVs imaged with widefield microscopy (*left*) and MuZIC (*right*). FOV (*i*) is centered on an area of sparsely labeled neurons, while FOV (*ii*) contains densely labeled cells. Individual neurons are difficult to identify with widefield imaging but easily discernable with MuZIC (representative of 5 animals). **b**. *In vivo* imaging of subthreshold membrane potential changes and spiking in layer 2/3 pyramidal neurons reveals correlated dynamics. Two example FOVs are shown (n=2 animals). Action potentials ride on top of subthreshold depolarizations, as expected. FOV coordinates represent axial distance from the pial surface to plane 1. **c**. Spontaneous activity simultaneously measured from cells distributed across four imaging planes (images representative of 34 fields, 5 animals).

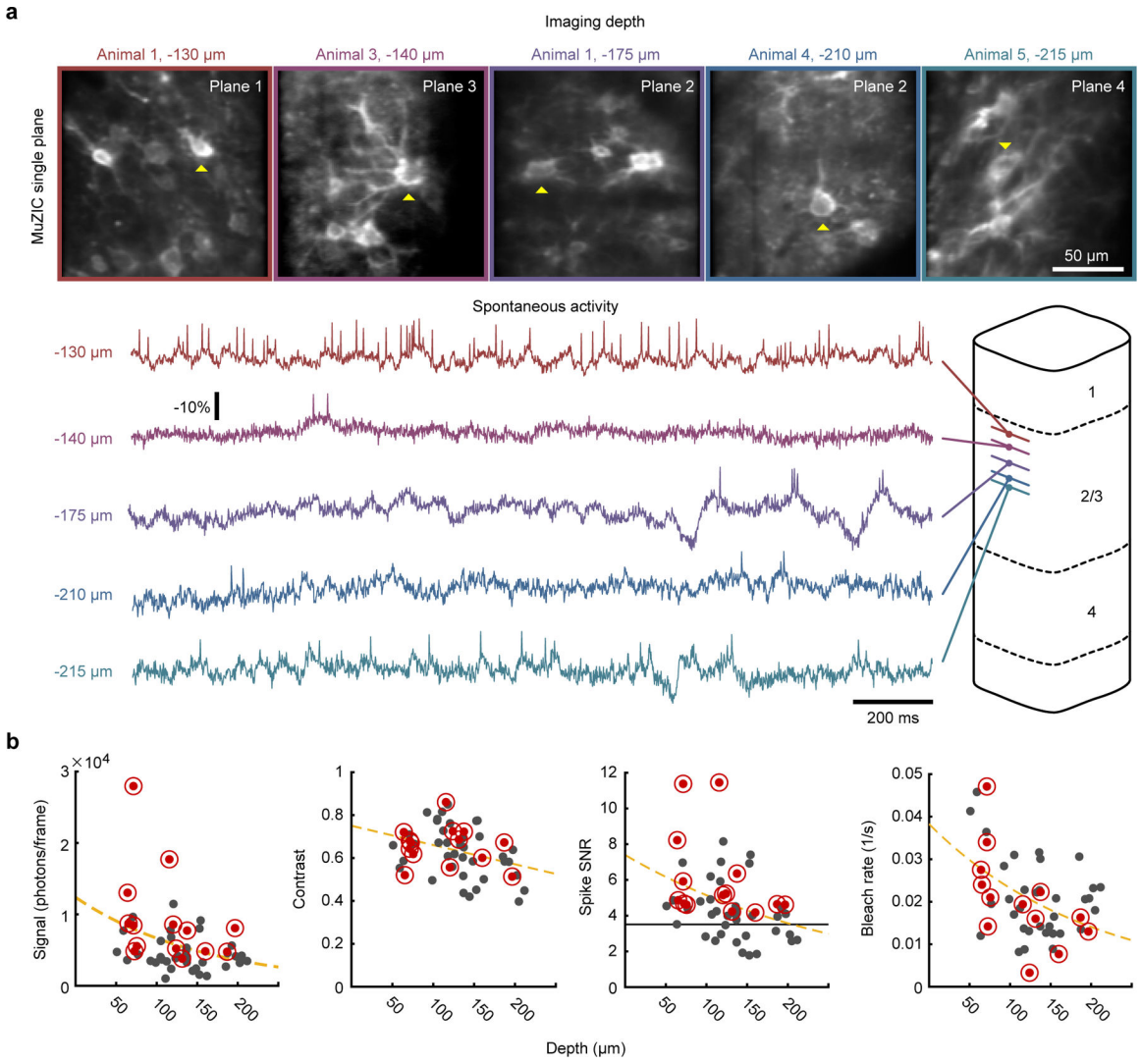

Figure 4 –. Depth dependence of imaging with *MuZIC*.

a. MuZIC can be used to detect spontaneous activity in neocortical layer 2/3 *in vivo*. Cells labeled with Voltron2-ST$_{JF552}$ at 5 axial depths (measured from pia to plane 1) show subthreshold dynamics and spiking in awake animals (*yellow arrows*, n=5 FOVs, 4 animals). Schematic illustrates depths at which MuZIC data were collected relative to cortical laminae.

b. Quantification of fluorescence, contrast, estimated spike SNR, and bleaching rate for all cells identified across all planes in the experiments depicted in Figs. 3b, c and 4a (n = 52 cells, 8 FOVs, 5 animals). Time series illustrated in Figs. 3b, c and 4a correspond to cells indicated in red.

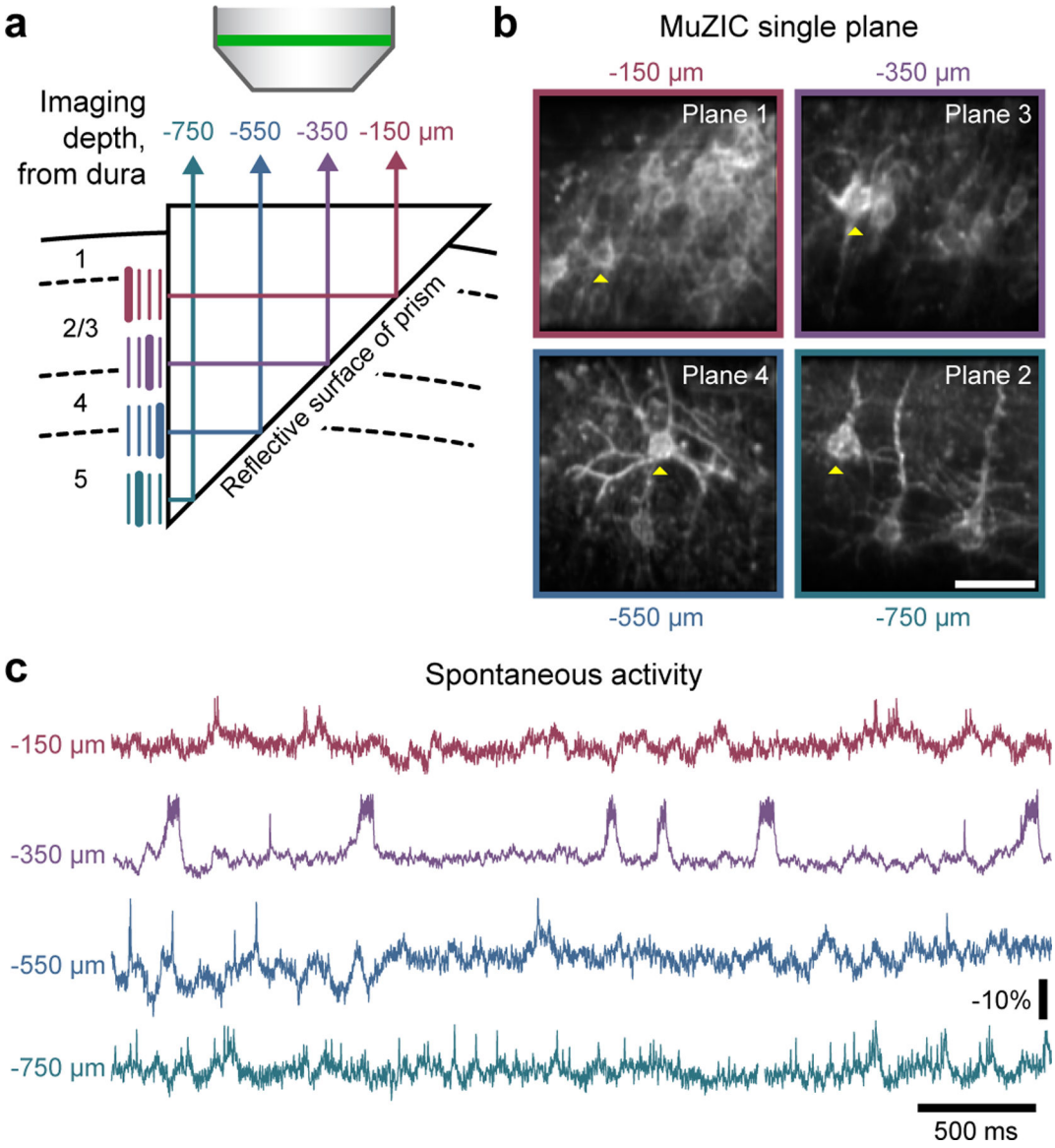

Figure 5 –. MuZIC can be performed through a microprism to visualize cells across cortical layers.

a. Schematic illustration of microprism positioning in the cortex and depths at which MuZIC data were collected through the prism. Images acquired across the horizontal face of the microprism arise from different depths along the vertical face of the prism. Highlighted imaging planes correspond to planes shown in (**b**). **b**. Single plane images collected across 4 depths in the cortex reveal neurons with varied morphology, including deep layer pyramidal neurons (*bottom right*, representative of 15 fields, 2 animals). Yellow arrows highlight cells whose membrane potential profiles are shown in (**c**). Scale bar, 50 µm. **c**. Examples of subthreshold and suprathreshold dynamics *in vivo* recorded from different penetration depths across all cortical layers.

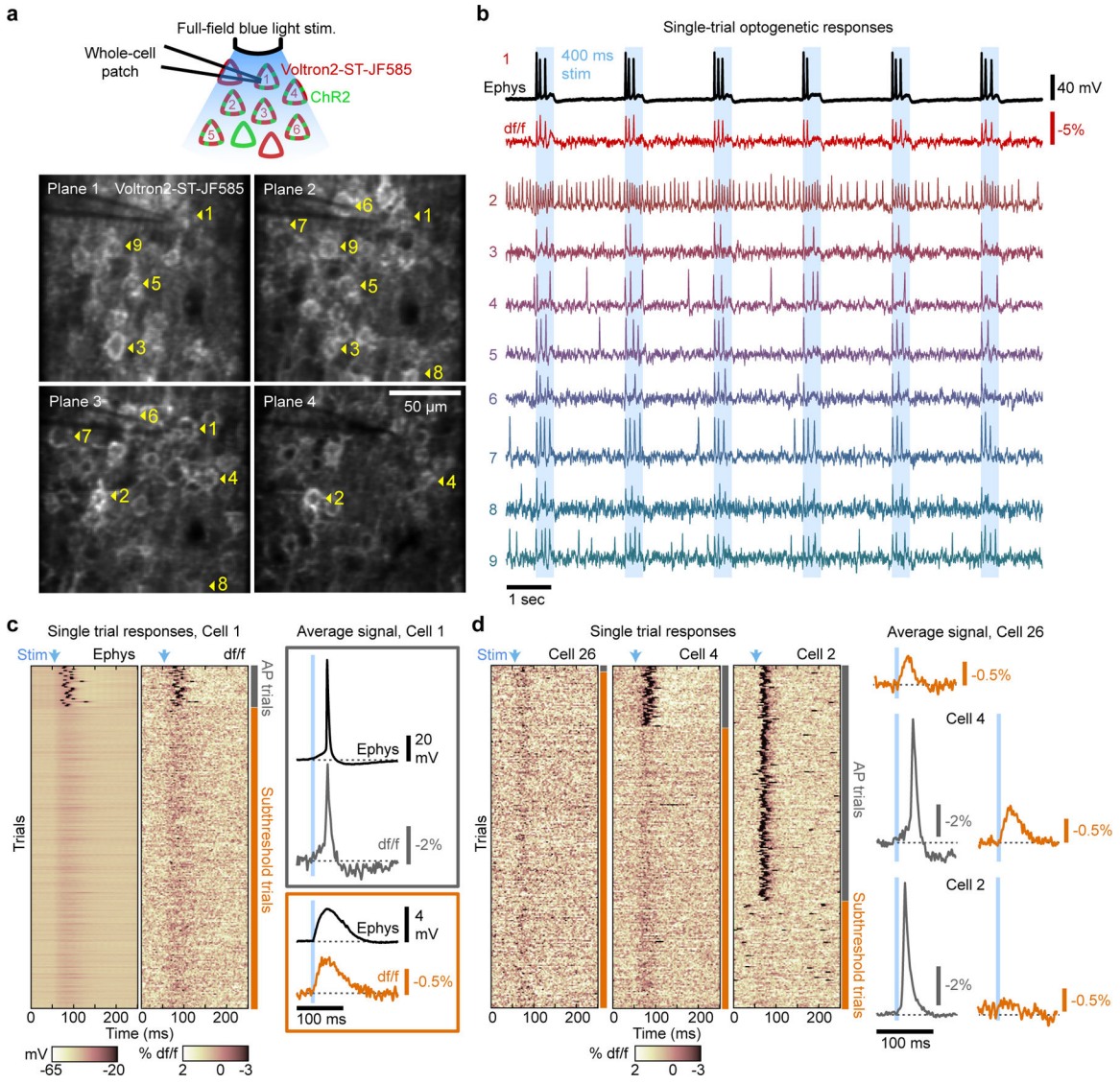

Figure 6 –. Simultaneous imaging and optogenetic stimulation with minimal optical crosstalk.

a. *Top,* Schematic of experiment. Overlapping subsets of neurons are virally labeled with Voltron2-ST$_{JF585}$ and ChR2. Widefield optical stimulation excites ChR2-expressing neurons. *Bottom,* Expression of Voltron2-ST$_{JF585}$ across four imaging planes (images representative of 16 fields, 2 animals). **b**. Simultaneous electrophysiological (*black*) and optical recording (*red*) of membrane potential from cell indicated by red ROI in (***a***) as well as optical recording from eight additional Chr2+/Voltron2-ST$_{JF585}$+ neurons in response to repeating 400-ms blue light stimuli. **c.** Short (0.5 ms) blue light stimuli induce action potentials (top, gray bars) or subthreshold voltage deflections (*bottom, orange bars*) in both electrophysiological (*left heatmap*) and optical (*right heatmap*) recordings of membrane potential. 256 repetitions shown. Average electrophysiological and optical recordings across all trials in which action potentials (*gray box, top*) or subthreshold depolarizations (*orange box, bottom*) were elicited. **d**. Optical recordings, as in (***c***) of additional cells from the same

field of view that displayed subthreshold responses (*left*) and action potentials on a minority (*middle*) and majority (*right*) of trials.